Journal of Biomedical Optics

SPIEDigitalLibrary.org/jbo

Optimizing the performance of dual-axis confocal microscopes via Monte-Carlo scattering simulations and diffraction theory

Ye Chen
Jonathan T. C. Liu

SPIE

Optimizing the performance of dual-axis confocal microscopes via Monte-Carlo scattering simulations and diffraction theory

Ye Chen and Jonathan T. C. Liu
Stony Brook University (SUNY), Department of Biomedical Engineering, Stony Brook, New York 11794

Abstract. Dual-axis confocal (DAC) microscopy has been found to exhibit superior rejection of out-of-focus and multiply scattered background light compared to conventional single-axis confocal microscopy. DAC microscopes rely on the use of separated illumination and collection beam paths that focus and intersect at a single focal volume (voxel) within tissue. While it is generally recognized that the resolution and contrast of a DAC microscope depends on both the crossing angle of the DAC beams, 2θ, and the focusing numerical aperture of the individual beams, α, a detailed study to investigate these dependencies has not been performed. Contrast and resolution are considered as two main criteria to assess the performance of a point-scanned DAC microscope (DAC-PS) and a line-scanned DAC microscope (DAC-LS) as a function of θ and α. The contrast and resolution of these designs are evaluated by Monte-Carlo scattering simulations and diffraction theory calculations, respectively. These results can be used for guiding the optimal designs of DAC-PS and DAC-LS microscopes. [DOI: 10.1117/1.JBO.18.6.066006]

Keywords: dual-axis confocal microscopy; line scanning; point scanning; Monte-Carlo simulation; diffraction theory; contrast; resolution; optical-sectioning microscopy.

Paper 130114R received Mar. 1, 2013; revised manuscript received Apr. 26, 2013; accepted for publication May 3, 2013; published online Jun. 3, 2013.

1 Introduction

Confocal microscopy, using point illumination and pinhole detection to reject out-of-focus and multiply scattered light from the object, provides improved imaging resolution and contrast over traditional microscopy and has become one of the most widely used biomedical optical imaging techniques.[1] In the past decade, various confocal microscope architectures have been developed for diverse biomedical applications.[2–15] A large objective lens with a high numerical aperture (NA) is generally utilized in a conventional confocal microscope to obtain high-resolution images. However, high-NA focusing leads to a short working distance due to geometric constraints. Therefore, the scan mirror must be placed prior to the objective which leads to off-axis aberrations that must be alleviated by the use of multiple corrective lenses, which further increases the objective size. Also, in a conventional single-axis confocal microscope, both the illumination and collection beams travel a common path in tissue, causing a significant amount of out-of-focus and multiply scattered light to be collected by the high-NA objective as background, thus decreasing imaging contrast and depth.[16–19] In the dual-axis confocal (DAC) microscope, two off-axis low-NA beams are aligned such that the illumination and collection beams intersect and focus at a single location within tissue. A long working distance results from utilizing low-NA lenses, which allows for a scanning mirror to be placed at the distal end of the objective to provide a large field of view without introducing scanning-induced aberrations.[20] Furthermore, since the illumination and collection beams travel different paths in tissue, the detector collects less out-of-focus and multiply scattered background light, thus leading to improved imaging depth and contrast.[12,16–19,21]

In this paper, we are interested in optimizing the imaging performance of two distinct DAC architectures. In point-scanned DAC microscopy (DAC-PS), a focused point is scanned through tissue in two dimensions to reconstruct an image pixel-by-pixel. In line-scanned DAC microscopy (DAC-LS), a focused line is scanned through tissue in only one dimension such that the image is reconstructed line-by-line. Instead of a single point detector, the line-scanned confocal microscope uses a one-dimensional linear-array detector to image an entire line at once, potentially improving the imaging speed and simplifying the scanning mechanism. However, there is a tradeoff in performance since confocality is lost in one dimension for a line-scanned DAC, which results in greater pixel crosstalk and diminished rejection of out-of focus and multiply scattered background light.[10,17–19,22,23]

Contrast and spatial resolution are two major performance parameters to consider when assessing optical-sectioning microscopes. Previous diffraction theory studies have shown that spatial resolution depends on both the crossing half angle of the dual-axis beams, θ, and the focusing NA of the individual beams, α.[21,24,25] It is also generally assumed that tissue-imaging contrast is a function of θ and α. However, this dependency has not been studied in great detail. Since diffraction theory does not account for any scattering events, Monte-Carlo simulations are therefore used in this study to characterize the tissue-imaging performance (contrast) of DAC-PS and DAC-LS configurations in reflectance mode as a function of θ and α. Here, contrast is defined as the ratio between the in-focus signal in an image and

Address all correspondence to: Jonathan T. C. Liu, Stony Brook University (SUNY), Department of Biomedical Engineering, Stony Brook, New York 11794. Tel: 631-632-1727; Fax: 631-632-3222; E-mail: jonathan.liu@stonybrook.edu

the background signal due to out-of-focus and multiply scattered light: the signal-to-background ratio (SBR). Furthermore, in order to provide a comprehensive guide for the design of these devices, we also include diffraction theory calculations of spatial resolution as a function of θ and α.

2 Experimental Methods

2.1 *Monte-Carlo Simulation*

2.1.1 *Software*

We used FRED software (Photon Engineering, Tucson, AZ) for all Monte-Carlo simulations. This Monte-Carlo model utilizes a Henyey–Greenstein approximation of Mie scattering theory.[26] The tissue model in this simulation has a scattering coefficient μ_s of 30 mm^{-1} and an anisotropy factor g, of 0.81.[27,28] These values are intended to mimic the scattering parameters measured in human skin at around 633 to 810 nm. In order to eliminate aberrations and reflections produced at the air–tissue interfaces and to simplify the simulation model, the index of refraction of the scattering media, n, is set as unity. Our Monte-Carlo simulations are designed to estimate tissue-imaging performance for various confocal configurations but do not take into consideration polarization, diffraction, and absorption. Furthermore, these simulations do not reflect other scattering events in real tissue, such as refractive beam steering and lensing introduced by heterogeneous structures that have dimensions larger than the operating wavelength of light (785 nm in this case). Nevertheless, Monte-Carlo simulations provide an excellent first-order approximation of optical-sectioning performance in tissues, which we have successfully validated through experiments with homogeneous scattering phantoms such as Intralipid.[12,29]

2.1.2 *Geometric model*

Figure 1 displays the geometric design used for DAC Monte-Carlo simulations. To model a DAC system with single-mode fibers serving as illumination and collection pinholes, two off-axis Gaussian beams with a $1/e^2$ focusing NA, α, are aligned such that they intersect at their foci with a crossing angle of 2θ. In particular, the illumination beam is created by a Gaussian point source at 785 nm with a numerical aperture α, which is imaged without magnification into tissue through a pair of matched aspheric lenses, $L1$ (Edmund Optics #47728) with a 22.5-mm focal length. The collection path is identical to the illumination path and symmetrical with respect to the z axis. For the DAC-LS configuration, a cylindrical lens ($C1$) with a 300-mm focal length is introduced into the illumination arm so that a focal line (~550 μm long) is generated in the y direction at the imaging plane.[10]

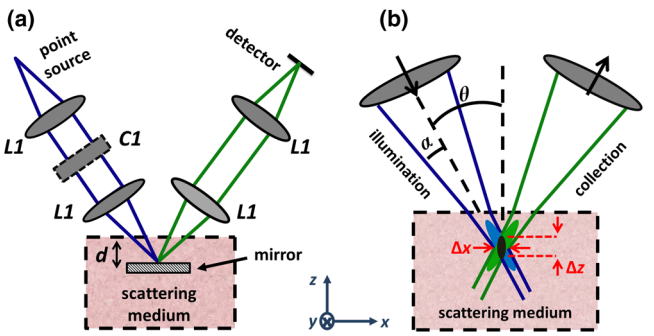

Fig. 1 (a) The DAC model used for Monte-Carlo simulations. (b) The focal region of a DAC microscope. In the DAC architecture, the illumination and collection beams intersect at one focal volume (black) with spatial resolution Δx and Δz.

2.1.3 *Procedure*

Since we aim to provide a guide to optimize the design of DAC microscopes, we vary θ and α in our Monte-Carlo simulations to analyze their effects on contrast and resolution. Based on our experience in building DAC microscope systems, we limit our analysis to a range of practical values: 0.1 rad $< \alpha <$ 0.25 rad and 15 deg $< \theta <$ 35 deg.[12,21,24] In order to investigate the effect of each variable independently, α is fixed at 0.11 rad (consistent with our previous simulation setup) when θ is changed.[12,17] Likewise, θ is kept at 30 deg when α is varied. Note that varying α causes the diffraction-limited spot size to change. Therefore, the pinhole size at the detector must be adjusted as α is altered.[21] For instance, when $\alpha = 0.1$ rad, we choose a pinhole size of 3×3 microns, which is slightly larger than the spot size calculated by diffraction theory. Since the diffraction-limited spot size scales with $1/\alpha$, if α is increased to 0.2 rad, the pinhole is reduced to 1.5×1.5 microns. In all simulations, our detector plane is oriented perpendicular to the collection beam and consists of pixels separated by 0.1 microns. Thus, a 3×3 micron pinhole corresponds to a 31×31 bin of detector pixels, whereas a 1.5×1.5 micron pinhole corresponds to a 16×16 bin of detector pixels.

2.1.4 *Signal-to-background ratio*

In order to measure the SBR of various DAC-PS and DAC-LS configurations, a mirror is placed at the focal plane and embedded within a homogenous scattering medium (Sec. 2.1.1). When the 100% reflective mirror is located exactly at the focus of the microscope, a peak signal is obtained. The peak signal is dominated by ballistic (nonscattered) photons but also contains a certain amount of background photons. We measure the background signal by removing the mirror from the simulation. As imaging depth increases, the SBR will decrease. Here, imaging depth is defined as the "perpendicular optical length," $L_p = 2\mu_s d$, which is a nondimensional quantity that refers to the total number of mean free paths that ballistic (nonscattered) photons travel in a perpendicular round-trip path between the tissue surface and the mirror.

2.2 *Diffraction Theory*

In our previous study, the full-width at half-maximum spatial resolution was calculated from diffraction theory,[24]

$$\Delta x = \frac{0.466\lambda}{n(\pi/2 \cdot \alpha)\cos\theta} \quad \Delta y = \frac{0.466\lambda}{n(\pi/2 \cdot \alpha)}$$
$$\Delta z = \frac{0.466\lambda}{n(\pi/2 \cdot \alpha)\sin\theta}. \tag{1}$$

For the DAC-PS configuration, Δy depends only on the focusing NA of the individual beams, α, and is not a function of crossing angle, θ. For the DAC-LS configuration, since the focal line extends in the y direction, Δy is also determined by how fully the linear array samples the line according to the Nyquist sampling criteria. Here, we focus our analysis on the

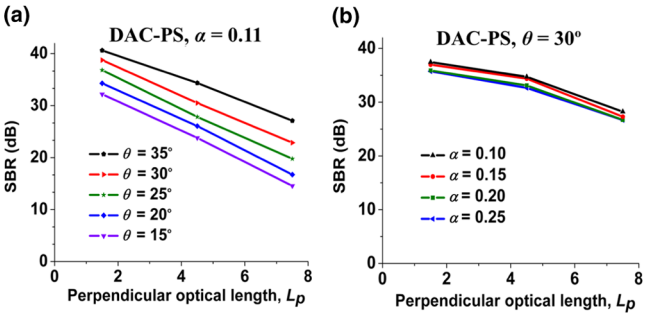

Fig. 2 The signal-to-background ratio (SBR) for the DAC-PS configuration as a function of imaging depth, L_p, when (a) varying θ with α fixed at 0.11 rad and (b) varying α with θ fixed at 30 deg.

spatial resolution in the x and z directions, which are functions of both θ and α, as seen in Eq. (1). In order to apply these calculations for all wavelengths, a nondimensional resolution is reported by normalizing against wavelength, λ: $\Delta x/\lambda$ and $\Delta z/\lambda$. Note that these resolution calculations apply for both the DAC-PS and DAC-LS designs.

3 Results

Our results indicate that the effects of θ and α on contrast and resolution are quite different for the DAC-PS versus DAC-LS architectures.

3.1 *DAC-PS*

Plots of SBR versus imaging depth (L_p) for the DAC-PS configuration are shown in Fig. 2. In Fig. 2(a), when α is fixed, increasing θ results in improved SBR at all depths. However, Fig. 2(b) shows that SBR is not sensitive to variations in α. These results indicate that maximizing θ is important for achieving high contrast (i.e., rejecting as much out-of-focus and multiply scattered light as possible) for the DAC-PS design, while varying α is not as important (see Sec. 4 for discussion).

3.2 *DAC-LS*

Plots of SBR versus imaging depth (L_p) for the DAC-LS configuration are shown in Fig. 3. Figure 3(a) indicates that increasing θ is not as important, compared to the DAC-PS configuration, for improving SBR, but increasing θ does make a slight difference in improving the contrast at shallow depths. Figure 3(b) suggests that varying α also plays a minor role in improving contrast. Note that for the DAC-LS configuration, overall SBR performance is worse than for the DAC-PS, as

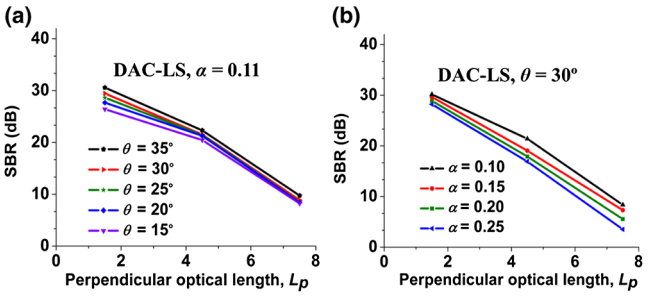

Fig. 3 The signal-to-background ratio (SBR) for the DAC-LS configuration as a function of imaging depth, L_p, when (a) varying θ with α fixed at 0.11 rad and (b) varying α with θ fixed at 30 deg.

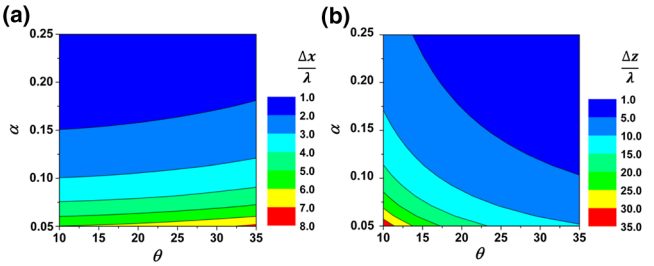

Fig. 4 Contour plots for nondimensional spatial resolution: (a) $\Delta x/\lambda$ and (b) $\Delta z/\lambda$. This figure applies to both the DAC-PS and DAC-LS configurations.

expected (see Introduction). Therefore, the DAC-LS would likely be utilized for imaging at shallow depths.

3.3 *Resolution*

The contour plots in Fig. 4 demonstrate the effect of θ and α on spatial resolution (x and z directions). Figure 4(a) implies that α contributes more than θ in determining Δx. In other words, high NA beams (large α) help to ensure high resolution in the x direction. However, for any given α, increasing θ only slightly improves Δx resolution. Figure 4(b) indicates that in order to achieve good resolution in the z direction, maximizing both θ and α is necessary.

4 Discussion and Conclusion

Our Monte-Carlo simulations and diffraction theory calculations suggest that the optimization of DAC configurations may require very different design parameters, depending upon the biomedical application of interest.

First, the dependencies of contrast on θ and α were evaluated by Monte-Carlo simulations. According to Fig. 2, SBR is more sensitive to θ than α. In particular, increased θ results in better SBR. An explanation for this result is that the illumination and collection paths move closer to each other when their half crossing angle, θ, decreases. As the two beams move closer to each other, the out-of-focus and multiply scattered photons generated by the illumination beam are more likely to scatter into the collection beam. Thus, increasing θ improves the SBR (contrast). When the focusing NA of each individual beam, α, increases, the illumination and collection beams also move closer to each other, which would worsen the SBR. However, since the diffraction-limited spot size is reduced when α is increased, the correspondingly smaller pinhole improves the rejection of out-of-focus and multiply scattered background light.[30–32] These two effects balance each other, which ultimately causes the DAC-PS to be relatively insensitive to changes in α.

Figure 3 displays the effect of varying θ and α on the contrast of the DAC-LS configuration. At shallow depths, maximizing θ results in a slight improvement in SBR, but this contrast improvement in the DAC-LS architecture is much less than that in the DAC-PS architecture. We hypothesize that this may be due to pixel crosstalk serving as the dominant source of background in the DAC-LS configuration. The lack of confocality in one dimension for the line-scanned approach creates crosstalk between pixels along the focal line at the detector. This crosstalk diminishes the DAC-LS architecture's ability to reject out-of-focus and multiply scattered background light and thereby limits the achievable contrast (SBR) of the line-scanned DAC.[17]

Although diffraction theory does not account for scattering events, it allows us to express spatial resolution as a function of θ and α. Monte-Carlo simulations along with diffraction theory calculations provide a comprehensive guide to optimize the DAC-PS and DAC-LS microscopes for various imaging applications. For a DAC-PS microscope, optimization should seek to balance both contrast and spatial resolution. Since increasing θ is more important than α for obtaining highest contrast for a DAC-PS microscope, optimizing the DAC-PS design should prioritize the beam crossing half angle, θ. Moreover, according to diffraction theory, given a maximized θ, increasing α would also be preferred for maintaining good Δx and Δz resolution. Increasing α only slightly reduces contrast for the DAC-PS design. For the DAC-LS design, since contrast is not overly sensitive to variations in either θ or α, its optimization should focus on obtaining high spatial resolution (x and z directions). In the x direction, good resolution requires maximizing α. In the z direction, increasing both θ and α improves resolution.

In practice, one's choice of θ or α is often limited by pragmatic concerns such as working distance and device size, as well as the position and size of the scanning mechanism. Generally, large crossing angles, θ, imply larger device sizes and/or shorter working distances. Large crossing angles, θ, and beam numerical apertures, α, may also create additional challenges for aberration-corrected optics and the index-matching of beams into tissues.[9,33,34]

Acknowledgments

We would like to acknowledge funding support from the National Institute for Biomedical Imaging and Bioengineering—R00 EB008557 (Liu), the National Institute of Dental and Craniofacial Research—R01 DE023497 (Liu), and the office of the Vice President for Research at Stony Brook University. The authors also thank Danni Wang and Steven Leigh for paper revisions.

References

1. J. B. Pawley, *Handbook of Biological Confocal Microscopy*, 3rd ed., Springer, New York (2006).
2. D. L. Dickensheets and G. S. Kino, "Micromachined scanning confocal optical microscope," *Opt. Lett.* **21**(10), 764–766 (1996).
3. G. J. Tearney, R. H. Webb, and B. E. Bouma, "Spectrally encoded confocal microscopy," *Opt. Lett.* **23**(15), 1152–1154 (1998).
4. Y. S. Sabharwal et al., "Slit-scanning confocal microendoscope for high-resolution in vivo imaging," *Appl. Opt.* **38**(34), 7133–7144 (1999).
5. J. Knittel et al., "Endoscope-compatible confocal microscope using a gradient index-lens system," *Optics Comm.* **188**(5–6), 267–273 (2001).
6. C. Pitris et al., "A GRISM-based probe for spectrally encoded confocal microscopy," *Opt. Express* **11**(2), 120–124 (2003).
7. C. MacAulay, P. Lane, and R. Richards-Kortum, "In vivo pathology: microendoscopy as a new endoscopic imaging modality," *Gastrointest. Endosc. Clin. N Am.* **14**(3), 595–620 (2004).
8. R. Kiesslich et al., "Confocal laser endoscopy for diagnosing intraepithelial neoplasias and colorectal cancer in vivo," *Gastroenterology* **127**(3), 706–713 (2004).
9. K. Carlson et al., "In vivo fiber-optic confocal reflectance microscope with an injection-molded plastic miniature objective lens," *Appl. Opt.* **44**(10), 1792–1797 (2005).
10. P. J. Dwyer, C. A. DiMarzio, and M. Rajadhyaksha, "Confocal theta line-scanning microscope for imaging human tissues," *Appl. Opt.* **46**(10), 1843–1851 (2007).
11. F. Jean, G. Bourg-Heckly, and B. Viellerobe, "Fibered confocal spectroscopy and multicolor imaging system for in vivo fluorescence analysis," *Opt. Express* **15**(7), 4008–4017 (2007).
12. J. T. C. Liu et al., "Efficient rejection of scattered light enables deep optical sectioning in turbid media with low-numerical-aperture optics in a dual-axis confocal architecture," *J. Biomed. Opt* **13**(3), 034020 (2008).
13. H. Makhlouf et al., "Multispectral confocal microendoscope for in vivo and in situ imaging," *J. Biomed. Opt* **13**(4), 044016 (2008).
14. J. T. C. Liu et al., "Point-of-care pathology with miniature microscopes," *Anal. Cell Pathol. (Amst)* **34**(3), 81–98 (2011).
15. J. M. Jabbour et al., "Confocal endomicroscopy: instrumentation and medical applications," *Annals Biomed. Eng.* **40**(2), 378–397 (2012).
16. L. K. Wong et al., "Improved rejection of multiply scattered photons in confocal microscopy using dual-axes architecture," *Opt. Lett.* **32**(12), 1674–1676 (2007).
17. Y. Chen, D. Wang, and J. T. C. Liu, "Assessing the tissue-imaging performance of confocal microscope architectures via Monte Carlo simulations," *Opt. Lett.* **37**(21), 4495–4497 (2012).
18. D. S. Gareau, S. Abeytunge, and M. Rajadhyaksha, "Line-scanning reflectance confocal microscopy of human skin: comparison of full-pupil and divided-pupil configurations," *Opt. Lett.* **34**(20), 3235–3237 (2009).
19. Y. G. Patel, M. Rajadhyaksha, and C. A. Dimarzio, "Optimization of pupil design for point-scanning and line-scanning confocal microscopy," *Biomed. Opt. Express* **2**(8), 2231–2242 (2011).
20. T. D. Wang et al., "Dual-axes confocal microscopy with post-objective scanning and low-coherence heterodyne detection," *Opt. Lett.* **28**(20), 1915–1917 (2003).
21. J. T. C. Liu et al., "Dual-axes confocal reflectance microscope for distinguishing colonic neoplasia," *J. Biomed. Opt.* **11**(5), 054019 (2006).
22. B. Simon and C. A. Dimarzio, "Simulation of a theta line-scanning confocal microscope," *J. Biomed. Opt.* **12**(6), 064020 (2007).
23. A. A. Tanbakuchi, A. R. Rouse, and A. F. Gmitro, "Monte Carlo characterization of parallelized fluorescence confocal systems imaging in turbid media," *J. Biomed. Opt.* **14**(4), 044024 (2009).
24. J. T. C. Liu et al., "Micromirror-scanned dual-axis confocal microscope utilizing a gradient-index relay lens for image guidance during brain surgery," *J. Biomed. Opt.* **15**(2), 026029 (2010).
25. W. Gong, K. Si, and C. J. Sheppard, "Optimization of axial resolution in a confocal microscope with D-shaped apertures," *Appl. Opt.* **48**(20), 3998–4002 (2009).
26. L. G. Henyey and J. L. Greenstein, "Diffuse radiation in the galaxy," *Astrophys. J.* **93**, 70–83 (1941).
27. T. Collier et al., "Determination of epithelial tissue scattering coefficient using confocal microscopy," *IEEE J. Sel. Top. Quant.* **9**(2), 307–313 (2003).
28. W. F. Cheong, S. A. Prahl, and A. J. Welch, "A review of the optical-properties of biological tissues," *IEEE J. Quantum Elect.* **26**(12), 2166–2185 (1990).
29. D. Wang, Y. Chen, and J. T. C. Liu, "A liquid optical phantom with tissue-like heterogeneities for confocal microscopy," *Biomed. Opt. Express* **3**(12), 3153–3160 (2012).
30. J. M. Schmitt, A. Knuttel, and M. Yadlowsky, "Confocal microscopy in turbid media," *J. Opt. Soc. Am. A, Optics, Image Sci. Vis.* **11**(8), 2226–2235 (1994).
31. R. Gauderon and C. J. Sheppard, "Effect of a finite-size pinhole on noise performance in single-, two-, and three-photon confocal fluorescence microscopy," *Appl. Opt.* **38**(16), 3562–3565 (1999).
32. J. A. Conchello and J. W. Lichtman, "Optical sectioning microscopy," *Nat. Methods* **2**(12), 920–931 (2005).
33. R. T. Kester et al., "High numerical aperture microendoscope objective for a fiber confocal reflectance microscope," *Opt. Express* **15**(5), 2409–2420 (2007).
34. M. Kyrish and T. S. Tkaczyk, "Achromatized endomicroscope objective for optical biopsy," *Biomed. Opt. Express* **4**(2), 287–297 (2013).